Structure of Water-in-Salt and Water-in-Bisalt Electrolytes

Structure of Water-in-Salt and Water-in-Bisalt Electrolytes[†]

Miguel Angel González[a], Hiroshi Akiba[b], Oleg Borodin[c,*], Gabriel Julio Cuello[a], Louis Hennet[d], Shinji Kohara[e], Edward J. Maginn[f], Lucile Mangin-Thro[a], Osamu Yamamuro[b], Yong Zhang[f], David L. Price[g] and Marie-Louise Saboungi[h,*]

[a] Institut Laue-Langevin, 71 avenue des Martyrs, 38042 Grenoble Cedex 9, France

[b] Institute for Solid State Physics, University of Tokyo, Kashiwa, Chiba 277-8581, Japan.

[c] Battery Science Branch, U.S. Army Combat Capabilities Development Command, Army Research Laboratory, Adelphi, Maryland 20783, USA

[d] ICMN, Université d'Orléans/CNRS, 45071 Orléans, France

[e] Research Center for Advanced Measurement and Characterization, National Institute for Materials Science, 1-2-1 Sengen, Tsukuba, Ibaraki 305-0047, Japan.

[f] Dept. of Chemical and Biomolecular Engineering, University of Notre Dame, Notre Dame, Indiana 46556, USA; Joint Center for Energy Storage Research, Argonne National Laboratory, Lemont, Illinois 60439, USA.

[g] CEMHTI, CNRS/Université d'Orléans, 45071 Orléans, France.

[h] IMPMC, Sorbonne Université/CNRS, 75252 Paris, France.

[*] E-mail: oleg.a.borodin.civ@army.mil; ml.saboungi@gmail.com

[†] Electronic supplementary information (ESI) available.

We report a systematic diffraction study of two "water-in-salt" electrolytes and a "water-in-bisalt" electrolyte combining high-energy x-ray diffraction (HEXRD) with polarized and unpolarized neutron diffraction (ND) on both H_2O and D_2O solutions. The measurements provide three independent combinations of correlations between the different pairs of atom types that reveal the short- and intermediate-range order in considerable detail. The ND interference functions show pronounced peaks around a scattering vector $Q \sim 0.5$ Å^{-1} that change dramatically with composition, indicating significant rearrangements of the water network on a length scale around 12 Å. The experimental results are compared with two sets of Molecular Dynamics (MD) simulations, one including polarization effects and the other based on a non-polarizable force field. The two simulations reproduce the general shapes of the experimental structure factors and their changes with concentration, but differ in many detailed respects, suggesting ways in which their force fields might be modified to better represent the actual systems.

Introduction

Concern about the safety and environmental impact of the non-aqueous electrolytes currently employed in Li-ion batteries had led to a re-examination of aqueous electrolytes, with a view to increasing their electrochemical stability window and hence enabling their use in batteries with high-voltage electrode couples and high energy density. In 2015 Suo *et al.*[1] demonstrated a battery with a "water-in-salt" (WIS) electrolyte, a concentrated aqueous solution of lithium bis(trifluoromethanesulfonyl)imide (LiTFSI) in which an operating window of 3 V was made possible by a solid-electrolyte interphase (SEI) formed by the electrochemical reduction of the salt at the anode surface. Subsequently, Suo *et al*[2] explored a "water-in-bisalt" (WIBS) electrolyte by adding 7 m of a second salt, lithium trifluoromethanesulfonate (LiOTf), to the 21 m solubility limit of LiTFSI, further expanding the electrochemical stability window. Recent development with halogen intercalation cathodes has demonstrated performance approaching that of state-of-the-art non-aqueous Li-ion batteries.[3]

These developments have stimulated a large number of numerical studies with Molecular Dynamics (MD) simulations[1,2,4,5,6,7,8,9,10,11] and quantum chemical calculations[1,2,8] to understand and optimize the relatively high Li^+ conductivity of these electrolytes despite their high viscosity, recalling Angell's concept of decoupling electrical and mechanical relaxation in polymer electrolytes.[12] For example, the MD simulations of Borodin *et al*.[1,2,4] suggest that the high Li^+ contribution to conductivity in the LiTFSI-H_2O electrolyte is partially attributed to high salt dissociation and fast $Li^+(H_2O)_4$ diffusion through the $Li^+(H_2O)_4$-rich nanodomain, while the negatively charged ionic framework relax much slower. However, the simulations of Zhang and co-workers[11] predict a more homogeneous liquid structure for the same electrolytes instead of water-rich and $TFSI^-$-rich domains. Furthermore, a hopping mechanism was suggested for the Li^+ conduction in the electrolytes.[13]

MD simulations provide detailed information on the structural and transport properties of electrolytes that are essential for their choice and optimization for use in advanced

batteries. The results are obviously dependent, however, on the ability of the force field to accurately capture intermolecular interactions. In conjunction with other experimental techniques such as NMR and FTIR, scattering experiments provide a powerful means for validating the models. We recently reported dynamical measurements on LiTFSI-H_2O WIS and LiTFSI-LiOTf-H_2O WIBS electrolytes with quasielastic neutron scattering[14] and compared the water dynamics with the slower structural relaxation of the ionic framework predicted by the MD of Borodin *et al.*[1,2,4] Similarly, diffraction experiments provide a stringent test of the structural predictions of the simulations. Here we report a systematic diffraction study of the same systems, LiTFSI$(H_2O)_{4.0}$, LiTFSI$(H_2O)_{2.64}$ and (LiTFSI$_{0.75}$LiOTf$_{0.25}$)$(H_2O)_{2.0}$. For convenience we refer to these as 13.9 m, 21 m and (21 m + 7 m) solutions, respectively.

The measurements were made with high-energy x-ray diffraction (HEXRD) and neutron diffraction with both unpolarized and polarized neutrons. The neutron measurements were made on equivalent compositions with H_2O and D_2O. X-ray diffraction emphasizes the heavier atoms while neutron diffraction is more sensitive to correlations involving the hydrogen atoms, but with different weights for H and D. Thus, the measurements provide three independent combinations of correlations between the different pairs of atom types. The solutions with H_2O and D_2O will have the same structure except for quantum differences[15] which will be negligible in the present context, so HEXRD measurements were made only on the samples with H_2O.

The diffraction data are compared with the results of MD numerical simulations with a polarizable force field and also, for the two WIS compositions, with those based on a non-polarizable force field. These provide a stringent validation of the simulations and suggest possible improvements to the force fields.

Some diffraction results on the WIS solutions have been published previously with neutron measurements of the peak at low scattering vector in D_2O solutions[4,16] and with x-ray measurements on H_2O solutions.[11] However, as noted above, neutron diffraction on H_2O and D_2O solutions and x-ray diffraction give very different results and it is important to

use all three on the same systems to get a comprehensive view of their structure. Also, to our knowledge these are the first diffraction results reported on a WIBS solution.

Experimental

Sample preparation

Sample preparation followed the procedures described in Refs. 1, 2. The components had the highest commercially available purities: LiTFSI: 99.95%, LiOTf: 99.995%, D_2O: >99.9% D, all from Sigma-Aldrich. The mixing was performed in a glove bag after drying the salts under vacuum at 100°C. The differences from the ideal chemical compositions were all less than 0.1%.

Neutron diffraction

Two neutron diffraction techniques were used in this work: unpolarized neutron diffraction measurements were made on the D4 instrument[17] at the Institut Laue-Langevin (ILL) in Grenoble, France, over a large Q range 0.3 - 20 Å^{-1}, and polarized neutron diffraction measurements on the D7 instrument,[18] also at ILL.[19,20] (Q is the amplitude of the scattering vector $= (4\pi/\lambda) \sin\theta$, where λ is the neutron wavelength and 2θ the scattering angle). With polarized neutrons it is possible to separate the coherent signal from the incoherent background, which is especially high, and not easy to correct, with hydrogenous samples; D7 has a restricted Q range, 0.2 - 3.8 Å^{-1}, but about twice better Q resolution over this range as shown in Fig. S1 of the Supplementary Information (SI).

For the measurements on D4, the samples were loaded into standard vanadium containers having an internal diameter of 6 mm and measured inside a cryofurnace at 313 ± 2 K. An incident wavelength of 0.496 Å was used. Raw data were grouped into uncorrected $I(Q)$ curves using the standard routines available in D4, and then corrected for background, normalized by a vanadium standard, and corrected for inelastic effects (Placzek corrections) using a set of Python functions integrated into a Jupyter notebook.

On D7 the incident wavelength was 3.168 Å and the samples were measured inside aluminum hollow cylinders giving a sample thickness of 0.5 mm for the solutions with H_2O and 1.0 mm for those with D_2O. The samples where then placed inside a standard orange cryostat and measured at 313 ± 2 K. Measured transmissions were around 0.88-0.90 for the samples containing light water and 0.92-0.94 for those containing heavy water. For each sample, spin-flip and non-spin-flip measurements were taken and used to extract the coherent and incoherent nuclear scattering.[18] The standard correction procedure (polarization efficiency calculation using an amorphous silica standard, background subtraction, detector efficiency normalization and absolute intensity determination from a vanadium standard and separation of the incoherent and coherent components) was applied using the routines available in the LAMP program at ILL.[21] The incoherent differential cross section can be compared with the expected theoretical value calculated from the atomic composition of the samples in order to check the consistency of the reduction procedure. It was found that for the samples with H_2O the levels of both coherent and incoherent scattering were in reasonable agreement with theory, but for those with D_2O the incoherent levels were about twice as large, which could indicate an H_2O contamination of about 2-3% during sample handling. The differential scattering cross section (in barn/steradian/atom) obtained from the data reduction procedure is related to the total interference function $F(Q)$:[22]

$$\frac{1}{N}\left[\frac{d\sigma}{d\Omega}(Q)\right] = F(Q) + \sum_{\alpha}^{n} c_{\alpha} b_{\text{coh},\alpha}^2 + \sum_{\alpha}^{n} c_{\alpha} b_{\text{inc},\alpha}^2, \tag{1}$$

where c_{α}, $b_{\text{coh},\alpha}$ and $b_{\text{inc},\alpha}$ are respectively the concentration, coherent and incoherent scattering length of chemical species α, n is the number of different chemical species, and

$$F(Q) = \sum_{\alpha,\beta}^{n} c_{\alpha} c_{\beta} b_{\text{coh},\alpha} b_{\text{coh},\beta} \left[S_{\alpha\beta}(Q) - 1\right], \tag{2}$$

where $S_{\alpha\beta}(Q)$ are the Faber-Ziman partial structure factors.[23] Here the different experimental data (x-rays and neutrons with H_2O or D_2O) are compared with each other and with the simulation results *via* the weighted average interference function

$$F(Q) = \frac{\sum_{\alpha,\beta}^{n} c_{\alpha} c_{\beta} b_{\text{coh},\alpha} b_{\text{coh},\beta} \left[S_{\alpha\beta}(Q) - 1\right]}{\sum_{\alpha,\beta}^{n} c_{\alpha} c_{\beta} b_{\text{coh},\alpha} b_{\text{coh},\beta}}. \tag{3}$$

The atomic concentrations and neutron scattering lengths[24] of each type of element for the three concentrations here studied are given in Tables S1, S2, and S3, respectively.

High-energy x-ray diffraction

HEXRD measurements were carried out at the BL04B2 beam line[25] at the SPring-8 synchrotron radiation facility. The energy of the incident x-rays was 61.2 keV. Each sample was loaded into a 2 mm-diameter quartz tube and measured for 2 h. at 25°C. The diffraction data were corrected for polarization, absorption, and background, and the contribution of Compton scattering was subtracted using standard analysis procedures.[26] The corrected data sets were normalized to extract the x-ray-weighted normalized $F(Q)$, given by Eqs. (2, 3) with the neutron scattering lengths replaced by atomic form factors. The atomic numbers of each type of element for the three concentrations are given in Tables S1, S2, and S3, respectively.

Force field development and MD simulation methodology

The many-body polarizable MD simulations utilized APPLE&P force field with the previously published functional form, combining rules and fitting methodology,[27] with one exception: a revised permanent charge – induced dipole scaling was used. The 1-2, 1-3 and 1-4 charge -induced dipole interactions were excluded using an atomic group scheme $[CF_3][SO_2][N-Lp][SO_2][CF_3]$ as previously described.[28] A detailed comparison of the $Li^+/TFSI^-$ interactions and code is given in Borodin et al.[28]. The water model was adopted from Starovoytov et al.[29] The Li^+ and $TFSI^-$ charges were +0.94e and -0.94e, respectively, in order to partially account for the reduced by 25% water model polarization from the gas-phase value to 1.0425 $Å^3$.[29]

The simulation methodology followed the procedures described in Refs. 1, 2 and is briefly described in the SI. The compositions of the MD simulation boxes is given in Table S4. To examine the sensitivity of the structure to the force field, a limited number of simulations were made with a modified force field in which water repulsion to the CF_3-group of $TFSI^-$ was reduced allowing closer approach of water to the $-CF_3$ part of anion as discussed in detail in Note 1 of the Supporting Information.

We attach to the Supporting Information a tar archive with all force field files and simulation code, making it possible to reproduce the results shown here. In the following,

this is referred to as the "polarizable" simulation, and the results with the original (version f1p) and modified (version f1w) force fields are denoted "Pol1" and "Pol2", respectively, in the figures.

The non-polarizable force field development and the simulation methodology followed the procedures described in Ref. 11. MD simulations were carried out using the package LAMMPS.[30] Parameters for the Li$^+$ cation were taken from the optimized potential for liquid simulations (OPLS) force field.[31] The general Amber force field (GAFF)[32] was used to describe TFSI$^-$ anion and the SPC/fw model[33] was used to describe water. The partial charges of Li$^+$ and TFSI$^-$ were scaled to ±0.8 e, respectively, to approximate the effect of charge transfer and polarizability in the bulk phase.[34] The long-range electrostatic interactions were calculated using the particle-particle particle-mesh (PPPM) method[35] with a real space cutoff of 12 Å. The same cutoff was also used for van der Waals interactions and a tail correction[36] was applied.

The performance of the non-polarizable simulation was validated against experimental properties including density, viscosity, self-diffusion coefficient and apparent transference number. All the calculated results agree with experimental value, suggesting that the applied nonpolarizable force field can describe the structure and dynamics of the studied mixtures with reasonable accuracy.[11,13]

Each simulation box was equilibrated for 2 ns in the isothermal-isobaric (NPT) ensemble to determine the density, followed by a 20 ns production run in the canonical ensemble (NVT). The convergence of the simulated density in the NPT simulation for the 20 m LiTFSI solution at 298 K is included in the SI (Figure S11). The temperature and pressure were controlled by the Nose-Hoover[37] and the extended Lagrangian approach[38] with a time constant of 100 fs. The pressure was fixed at one atmosphere in all NPT simulations with isotropic volume fluctuations. In the following, this is referred to as the "non-polarizable" simulation, and the results are denoted "Fix" in the figures and tables.

The compositions of the simulation boxes for both polarizable and non-polarizable MD are summarized in Table S4, along with the densities of the simulations and experimental densities. It can be seen that the non-polarizable simulation reproduces the experimental densities, for reasons given above, while the polarizable one tends to underestimate it by about 4% for the original version (f1p) of the force field and instead agrees well (only a slight overestimation of 0.6%) for the revised version (f1w).

Experimental results

The full set of experimental results is shown in Fig. 1, where the weighted average interference functions for the three compositions for x-ray and neutron (from H_2O and D_2O solutions) measurements are shown. As expected, the main changes are observed at low Q (Fig. 1, left), reflecting changes in the intermolecular correlations with increasing salt concentration. On the left side of Fig. 1 only the D4 data are shown, while on the right side the results obtained in D4 and D7 can be compared to assess their consistency. Overall, the agreement between the unpolarized neutron diffraction measurements on D4 and the polarized neutron diffraction measurements on D7 is reasonably good, even for the samples with H_2O, despite the large incoherent scattering contribution. The low-Q features are better resolved in D7, as the resolution is about twice as good. Since the incoherent scattering is an order of magnitude larger than the coherent at low Q for the samples with H_2O and, as noted above, larger than predicted for the samples with D_2O, discrepancies between the D4 and D7 results due to difficulties in subtracting the self-scattering are not unexpected.

There are dramatic differences between the three sets of data, reflecting the heavy influence of the weighting scheme in the shape of the interference function and therefore the
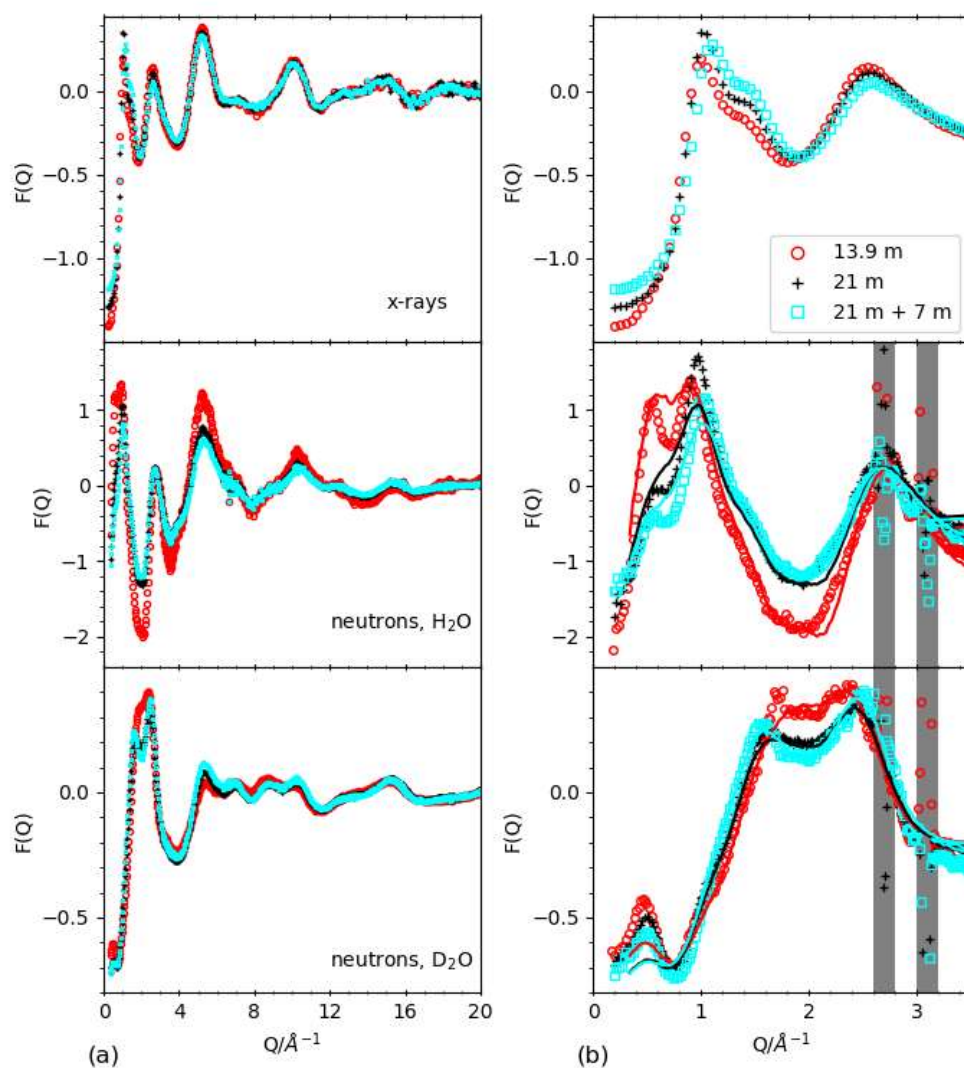
Fig. 1. Weighted average interference function $F(Q)$ for 13.9 m LiTFSI, 21 m LiTFSI and (21 m LiTFSI + 7 m LiOTf) solutions derived from HEXRD measurements at SPring-8 (top panels), neutron diffraction on H_2O solutions (middle panels), and neutron diffraction on D_2O solutions (bottom panels). Left side: full Q range; only D4 data are shown in the middle and bottom panels. Right side: blow-up of the low-Q region, where the main changes in $F(Q)$ with increasing salt concentration are observed; in the middle and bottom panels, data from both polarized neutron diffraction measurements on D7 (symbols) and unpolarized neutron diffraction on D4 (continuous lines with the same colors) are shown. The shaded area indicates the regions where the presence of aluminum Bragg peaks from the container make the D7 results unreliable.

additional gain of information obtained by the combination of both probes and the isotopic substitution. A remarkable feature is that the x-ray weighted average $F(Q)$ just shows mild and continuous changes with concentration, while the neutron results for the H_2O solutions show a strong variation in the relative intensities of the first two peaks. Neutron measurements on the D_2O solutions exhibit an intermediate behavior, with clear differences between the 13.9 m and the 21 m concentrations, while the addition of the LiOTf does not seem to have a large effect.

Only the neutron sets show clear features below 0.5 Å^{-1}, reflecting some intermediate-range order and usually accounted as some kind of nano-segregation due to the alternation of polar-apolar regions in ionic liquids[39] or alcohols.[40,41] In the D_2O solutions, this manifests as a clear low-Q peak at ≈ 0.46 Å^{-1} for the 13.9 m system, which shifts to ≈ 0.49 Å^{-1} and decreases in intensity at 21 m. Addition of LiOTf does not cause any noticeable peak shift, but its intensity is further decreased. In the H_2O solutions, there is a low-Q peak at ≈ 0.54-0.55 Å^{-1}on the shoulder of the main peak at around 0.9 Å^{-1} with comparable magnitude. The intensity of this peak decreases strongly when increasing the concentration to 21 m, while there is a further decrease, but not so pronounced, with the addition of 7 m LiOTf, without clear changes in the peak position.

The x-ray data do not show any marked feature below 1 Å^{-1} but instead show a first peak between 1.0 and 1.1 Å^{-1}, shifting slightly to large Q with increasing salt content, followed by a broad peak or shoulder at ≈ 1.4 Å^{-1} that also shifts to larger Q and increases its intensity with the addition first of LiTFSI and then of LiOTf. The behavior of the x-ray peak observed at about 1 Å^{-1} bears some resemblance with that of the main peak observed in the neutron data for H_2O solutions, with the peak first shifting from ≈ 0.90 (13.9 m) to ≈ 0.97 Å^{-1} (21 m) and gaining intensity, and then shifting again to larger $Q \approx 1.03$ Å^{-1} (21 m + 7 m) but losing intensity. However, given the complexity of the system (there are 36 different partial structure factors $S_{\alpha\beta}(Q)$ for the LiTFSI solutions and 78 for the (LiTFSI+LiOTf), it is impossible to say if this is just a coincidence or has a more profound meaning. On the other hand, the D_2O solutions do not show any prominent feature around

1 Å^{-1}, just a barely visible shoulder, but a double peak at $\approx$ 1.7 and $\approx$ 2.4 Å^{-1} for the 13.9 m solution. Then, curiously, the first one shifts to lower Q with increasing concentration ($\approx$ 1.6 Å^{-1} for 21 m and $\approx$ 1.55 Å^{-1} for (21 m + 7 m), while the second shifts to larger Q ($\approx$ 2.45 Å^{-1} for 21 m and $\approx$ 2.5 Å^{-1} for (21 m + 7 m).

Beyond 3 Å^{-1}, the structure is relative insensitive to the concentration, as intramolecular correlations become more dominant. This is especially visible in the x-ray data set, while the neutron data show some small but clear differences with concentration in the Q-region 5-6 Å^{-1}. Those differences are particularly pronounced in the H_2O solutions.

It is important to remember that the neutron scattering coherent length of natural hydrogen is -3.739 fm while that of deuterium is 6.671 fm, implying that all the partial structure factors $S_{\alpha\beta}(Q)$ involving hydrogen except $S_{HH}(Q)$ will change sign. Thus, the large variations with concentration observed in the weighted average function could indicate a significant rearrangement of the water network. However, as mentioned above, given the complexity of the structure and the large number of different atomic correlations contributing to the measured interference function, the only way to go beyond a qualitative discussion of the features observed is to make recourse to modeling. Thus, we have compared our experimental results with the molecular and ionic partial structure factors predicted by the MD simulations, which we now discuss.

Experiment-MD comparison

A detailed comparison of our experimental results for the 21 m solution with those derived from the polarizable and non-polarizable MD simulations is shown in Fig. 2. Similar comparisons for the 13.9 m LiTFSI and (21 m LiTFSI + 7 m LiOTf) solutions are shown in Figs. S2 and S3, respectively, of the SI. While a reasonable agreement between simulation and experiment is observed, it appears also clearly that none of the MD simulations reproduce consistently the full set of data, with some noticeable discrepancies.
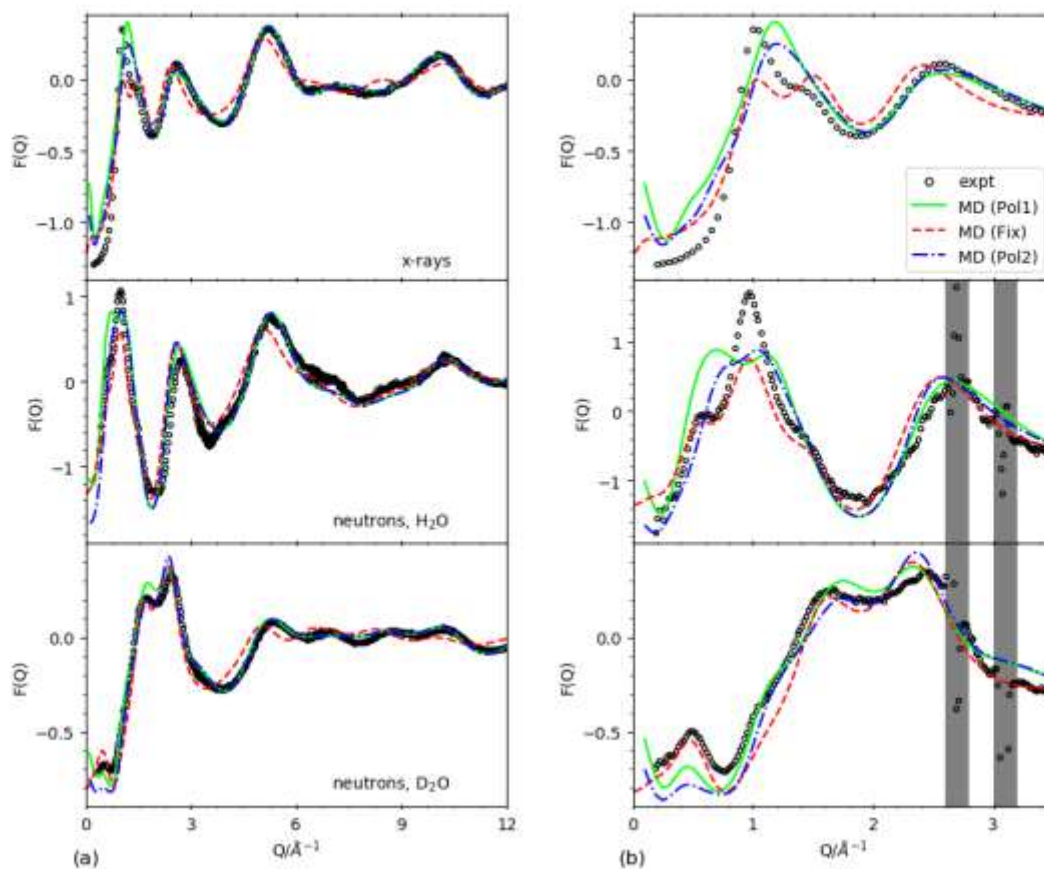
Fig. 2. Comparison of the experimental weighted average $F(Q)$s for the 21 m solution derived from HEXRD measurements at SPring-8 (top panels), neutron diffraction on H_2O solutions (middle panels), and neutron diffraction on D_2O solutions (bottom panels) with those derived from the original (Pol1) and modified (Pol2) polarizable simulations and from the non-polarizable simulation (Fix, 20 m concentration). Left side: extended Q range showing the more relevant features; for simplicity, in the middle and bottom panels only the experimental results obtained on D4 are shown, and the MD results have been smeared by the instrument resolution: Fig. S4 shows the effect of applying such smearing. Right side: blow-up showing the low-Q region, where the main differences between experiment and MD are observed; in the middle and bottom panels, only data from D7 are shown, and no smearing is applied to the MD results.

The polarizable simulations (Pol1 and Pol2) exhibit a very good agreement beyond ≈ 4 Å^{-1}, implying that the real-space correlation functions describing short-range interactions up to about 3 Å will also agree, but they have problems in reproducing the low-Q features that are sensitive to intermediate- and long-range interactions. It is precisely in this low-Q

regime where the agreement between experiment and simulation changes strongly from one data set to another. While the features observed on the D7 diffraction pattern for the D_2O solution are nicely reproduced (although with the intensity of the peak at 0.5 Å^{-1} slightly underestimated), the comparison of the data for the H_2O solution is clearly less encouraging: significant differences are observed over the Q range 0.2 - 2 Å^{-1}. The x-ray data exhibit an intermediate situation. The simulations with the modified force field (Pol2) produce some small changes in the interference function in the range 0 - 2.5 Å^{-1}, but no clear improvements in the overall agreement.

The non-polarizable simulations (Fix) also cannot reproduce all the features below $Q \approx 2$ Å^{-1} and obvious differences appear at higher Q. They match quite well the structure of the 21 m D_2O solution below 4 Å^{-1}, including the position and intensity of the low-Q peak at 0.5 Å^{-1}, although they miss the shoulder observed at ≈ 1.1 Å^{-1}. They reproduce quite well the first peak position of the x-ray weighted average $F(Q)$ but underestimate its intensity. They overestimate the intensity in the high-Q side of the 1.5 Å^{-1} shoulder. The position of the shoulder is moved to higher Q and the following peak at $Q \approx 2.5$ Å^{-1} is moved to lower Q by about 0.1 Å^{-1}. Here again large differences are observed for the H_2O solution. Although the simulations reproduce reasonably well the shape of the double peak, they clearly underestimate the intensity of the maximum. Beyond 2 Å^{-1}, clear differences in the intensities and positions of the peaks are observed, pointing to issues in correctly reproducing the local structure.

Similar findings are obtained when exploring the lower concentration (Fig. S2) or the (21 m LiTFSI + 7 m LiOTf solution) (Fig. S3), for which only the polarizable simulations are available.

Despite these discrepancies, it should be noted that the polarizable simulations – the only ones for which we have results for all three concentrations – are able to capture nicely many qualitative trends observed with increasing salt content. This can be gauged by comparing the experimental curves plotted in Fig. 1 with the equivalent results calculated

from the simulations shown in Fig. S5. While for the x-ray data the simulation is not able to capture the shoulder of the first diffraction peak, it mimics well the shift of this peak as well as the shift and small intensity decrease of the second peak around 2.5 Å^{-1}, and even the increase of intensity at low Q. The same is found for the D_2O solutions: as in the neutron result, the simulation predicts a noticeable variation on passing from 13.9 m to 21 m and much smaller changes when adding LiOTf. Also, the increases in intensity of the shoulder at ≈ 1.2 Å^{-1} and the peak at ≈ 5.5 Å^{-1} with increasing salt content are well reproduced. Only the variation of the low-Q peak is less well captured. Finally, on the H_2O solutions, where the effects due to salt concentration are much stronger, the simulation reproduces well the decrease in intensity of the lower-Q peak of the double peak structure with increasing salt content and the marked difference between the 13.9 m concentration and the two higher ones, both in the minimum at ≈ 1.9 Å^{-1} and the intensity of the peak at ≈ 5.3 Å^{-1}.

Partial structure factor analysis

MD simulations can provide a wealth of information, including all the separate partial structure factors contributing to the weighted average interference functions shown in Fig. 2. However, due to the large number of partials (36 for the LiTFSI solutions and 78 for LiTFSI+LiOTf), it is impossible to relate the most salient experimental features to just a few relevant partial structure factors. Therefore, to simplify the representation we follow Zhang *et al.*[11] in grouping the atomic partials by molecular groups: Li^+, $TFSI^-$, water, OTf^-. The results for the 21 m LiTFSI solution are shown in Fig. 3, where the partials predicted by the polarizable and non-polarizable simulations are compared for each set of weighting factors: x-ray, and neutron with H_2O and D_2O solutions. We confine our discussion to the low-Q region where, as noted above, the two simulations predict very different behavior. Figure 3 demonstrates that the x-ray data are dominated by the $TFSI^-$-$TFSI^-$ correlations and $TFSI^-$-H_2O anticorrelations, with H_2O-H_2O interactions playing a smaller, but non-negligible role. As expected, the contributions of lighter elements – Li and H/D – are enhanced in neutron diffraction. $TFSI^-$-$TFSI^-$ correlations still dominate the signal for the H_2O solution, but now H_2O-H_2O correlations contribute as a strong negative signal,
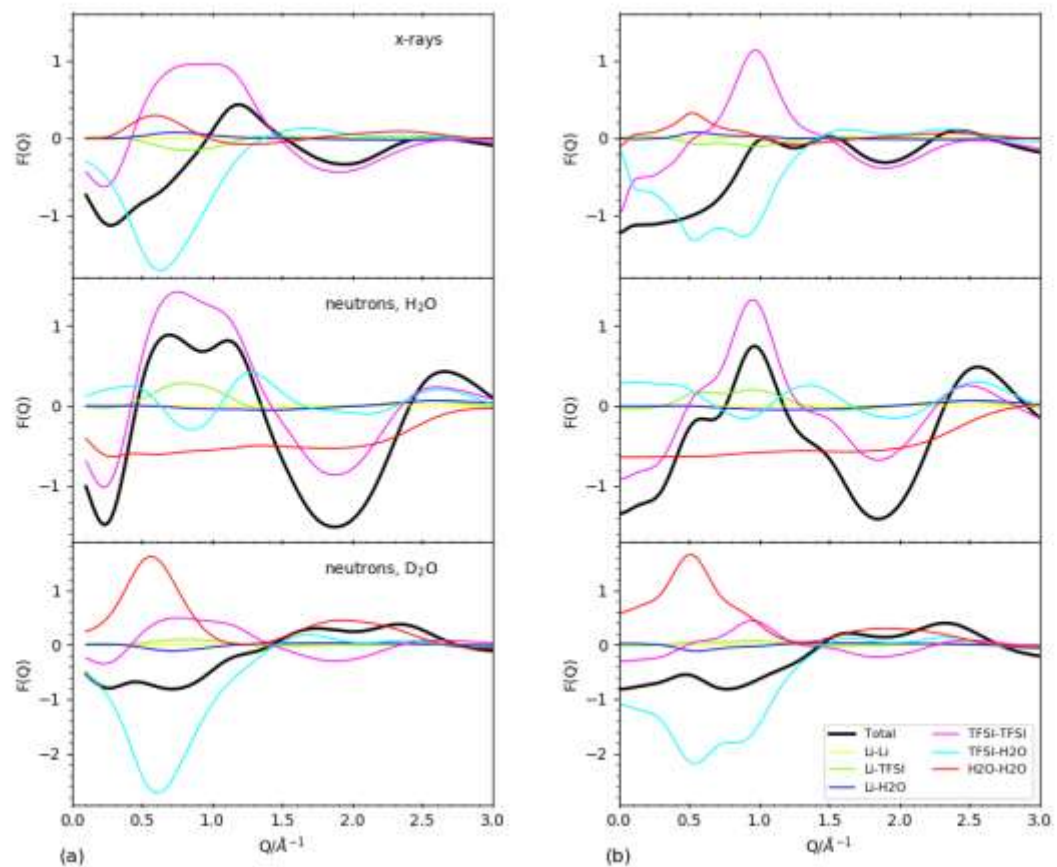
Fig. 3. Contributions to the x-ray (top panels) and neutron weighted average interference functions for H_2O (middle panels) and D_2O (bottom panels) for different molecular/ionic pairs showing the contributions of each partial to the MD weighted average $F(Q)$s shown in Fig. 2 and replotted here as solid thick lines. Left: results from the polarizable simulations for the 21 m solutions; right: results from the non- polarizable simulations for the 20 m solutions.

although relatively featureless below 2 Å^{-1}, and Li$^+$-TFSI$^-$ correlations become more visible and change sign with respect to the x-ray data due to the negative neutron coherent scattering length of Li$^+$. In the D_2O solution the signal is dominated by the D_2O-D_2O and TFSI$^-$-D_2O correlations, with the TFSI$^-$-TFSI$^-$ contribution becoming much less important than in the other two sets of weightings.

A comparison of the results obtained from the analysis of the trajectories from the polarizable (Fig. 3, left) and non-polarizable (Fig. 3, right) simulations indicates that the two sets agree regarding the dominant contributions in each experimental configuration but differ noticeably in the shape of the Q dependence. In the x-ray simulations, the dominant TFSI$^-$-TFSI$^-$ contribution to the main peak is broadened in the polarizable simulation results, masking the structure with a maximum at 1.0 Å^{-1} and shoulder at 1.5 Å^{-1} observed in the x-ray data. On the other hand, in the case of the non-polarizable simulation, the anti-correlated structure of TFSI$^-$-TFSI$^-$ and TFSI$^-$-H$_2$O partials results in a double peak structure that does not agree with the experimental observation either. In the neutron simulations of H$_2$O solutions, the TFSI$^-$-TFSI$^-$ contribution is also the dominant contribution to the main peak and broadened in the polarizable simulation results, which combined with the negative TFSI$^-$-H$_2$O contribution leads to a double peak, in contrast to the structure with a smaller peak on the low-Q side observed both in the experimental data and the weighted average $F(Q)$ from the non-polarizable simulation. The partial structure factors are quite different in the neutron simulations on D$_2$O solutions, dominated now by the positive D$_2$O-D$_2$O and compensating negative TFSI$^-$-D$_2$O in the polarizable simulation, reducing the height of the low-Q peak in the weighted average $F(Q)$. The height is higher in the weighted average $F(Q)$ from the polarizable simulation, approaching now the intensity observed in the D7 measurement. Analogous results are obtained for the 13.9 m LiTFSI solution, shown in Fig. S6.

The addition of the second salt, LiOTf, complicates the comparison since the number of molecular/ionic pairs increases substantially (Fig. S7). The pronounced increase of the TFSI$^-$-TFSI$^-$ and OTf$^-$-OTf$^-$ contributions at low Q, together with the negative signal for TFSI$^-$-OTf$^-$, suggest an intermediate-range ordering between the two anions. To evaluate the effects of concentration in the different partials we therefore combine the two anions into a single group and show in Fig. S8 the evolution of the six resulting partials using the weights corresponding to the neutron measurement in H$_2$O. The addition of the LiOTf is seen to have rather small effects apart from a rise in the anion-anion contribution at about 0.2 Å^{-1}, resulting from the intermediate-range ordering just discussed. It also gives rise to the bump at very low Q observed in the MD neutron weighted average for the H$_2$O solution

observed in Fig. S3 (middle right panel) but not seen in the experimental data, suggesting that the simulation is over-estimating the extent of this ordering.

Finally, the effects of the modified potential in the polarizable simulations for the 21 m solutions are shown in in Fig. S9, where the contributions of the different molecular/ionic pairs are compared for the original and revised force field. The H_2O-TFSI⁻ partials display the largest changes, due to the modified TFSI⁻–H_2O repulsion in the force field, which also results in minor changes of the TFSI⁻-TFSI⁻ packing.

Conclusions

As mentioned in the introduction, diffraction experiments provide a powerful test of the structural predictions of MD simulations. As is clear from the previous discussion, the two simulations with which we compare our results here reproduce the general shapes of the experimental structure factors and their changes with concentration but differ in many detailed respects. The differences are, however, quite unlike in the two simulations. This is in contrast, for example, with our study of an aqueous solution of an ionic liquid[42,43], where the MD predictions were in excellent agreement with the HEXRD data, both derived with the same procedures as in the present work.

Looking at the MD-experiment differences in detail, a broadened TFSI⁻-TFSI⁻ contribution to the peak around 1.0 Å⁻¹ in the results of the polarizable simulation appears to be masking the structure of this peak observed in the x-ray and neutron averages for the H_2O solutions, while an increased TFSI⁻-D_2O contribution may be suppressing the low-Q peak in the neutron average for the D_2O solution. The results of the non-polarizable simulation appear to be in better agreement for the neutron-weighted $S(Q)$ but not for the X-ray weighted. There are also deviations from the experimental data at 3.0 Å⁻¹ and higher Q values. We hypothesize these are due to the C-S and N-S bond lengths in the model for TFSI⁻ being slightly different from those obtained when optimizing the structure of TFSI⁻ with highly accurate quantum calculations. These small effects do not appear in the low-Q structure but are likely causing the differences with experiment at high Q. Overall, because the long-

range packing structure in these electrolytes is illustrated by the low-Q region of $F(Q)$, the comparisons shown in this work suggest that the homogeneous picture predicted by the non-polarizable simulation is likely more accurate.

To guide future work on the structure of complex molecular systems, we derive the following general conclusions from this work:

1. While MD simulations are essential for deriving meaningful insights from diffraction measurements, the force fields currently in use still have significant limitations. While they provide much useful information, they are far from perfect in reproducing the full structure of the complex systems studied here, suggesting that there is room for improvement.

2. Accurate experimental data are needed for benchmarking reliable force fields. Here it is important to use more than one set of experimental data. Many possible structures will be compatible with a single set, but adding additional data imposes constraints that are more demanding.

3. Neutrons are an essential probe of the structure of aqueous solutions, especially when polarized neutrons are available, and should be used in conjunction with H:D substitution to complement x-ray measurements.

We hope that these observations will be helpful in developing more accurate force fields in future work on these and other complex systems.

Conflicts of interest

There are no conflicts to declare

Acknowledgements

measurements were carried out at the Institut Laue-Langevin, Grenoble, France. The modeling was supported by the U.S. Department of Energy, Office of Science, Basic Energy Sciences Joint Center for Energy Storage Research, under Cooperative Agreement W911NF-19-2-0046 and Contract DEAC0206CH11357. YZ and EM thank the Center for Research Computing (CRC) at the University of Notre Dame for providing computational resources.

The neutron scattering data are publicly available at doi: 10.5291/ILL-DATA.6-02-593, doi: 10.5291/ILL-DATA.EASY-633.

[†]Supplementary Information

We attach a text file (SI WIS and WIBS March 31 2022-1.pdf) containing additional figures and tables in support of this paper and a tar archive (LiTFSI-2p7H2O-f1p-298K.tar) containing all files used for the polarizable simulations including the force field files and MD simulation code.

References

[1] L. Suo, O. Borodin, T. Gao, M. Olguin, J. Ho, X. Fan, C. Luo, C. Wang and K. Xu, Water-in-salt" electrolyte enables high-voltage aqueous lithium-ion chemistries, *Science,* 2015, **350**, 938-943.

[2] L. Suo, O. Borodin, W. Sun, X. Fan, C. Yang, F. Wang, T. Gao, Z. Ma, A. Schroedervon Cresce, S. M. Russell, M. Armand, A. Angell, K. Xu and C. Wang, Advanced High-Voltage Aqueous Lithium-Ion Battery Enabled by "Water-in-Bisalt" Electrolyte, *Angew. Chem. Int. Ed.,* 2016, **55,** 7136–714.

[3] C. Yang, J. Chen, X. Ji, T. P. Pollard, X. Lü, C.-J. Sun, S. Hou, Q. Liu, C. Liu, T. Qing, Y. Wang, O. Borodin, Y. Ren, K. Xu and C. Wang, Aqueous Li-Ion Battery Enabled by Halogen Conversion–Intercalation Chemistry in Graphite, *Nature,* 2019, **569,** 245-250.

[4] O. Borodin, L. Suo, M. Gobet, X. Ren, F. Wang, A. Faraone, J. Peng, M. Olguin, M. Schroeder, M. S. Ding, E. Gobrogge, A. von Wald Cresce, S. Munoz, J. A. Dura, S. Greenbaum, C. Wang and K. Xu, Liquid Structure with Nano-Heterogeneity Promotes Cationic Transport in Concentrated Electrolytes, *ACS Nano,* 2017**, 11**, 10462-10471.

[5] J. Lim, K. Park, H. Lee, J. Kim, K. Kwak and M. Cho, Nanometric Water Channels in Water-in-Salt Lithium Ion Battery Electrolyte, *J. Am. Chem. Soc.,* 2018, **140**, 15661–15667.

[6] Z. Li, R. Bouchal, T. Mendez-Morales, A. L. Rollet, C. Rizzi, S. Le Vot, F. Favier, B. Rotenberg, O. Borodin, O. Fontaine and M. Salanne, Transport Properties of Li-TFSI Water-in-Salt Electrolytes, *J. Phys. Chem. C,* 2019, **123**, 10514-10521.

[7] Z. Yu, L. A. Curtiss, R. E. Winans, Y. Zhang, T. Li and L. Cheng, Asymmetric Composition of Ionic Aggregates and the Origin of High Correlated Transference Number in Water-in-Salt Electrolytes, *J. Phys. Chem. Lett.,* 2020, **11**, 1276-1281.

[8] K. S. Han, Z. Yu, H. Wang, P. C. Redfern, L. Ma, L. Cheng, Y. Chen, J. Z. Hu, L. A. Curtiss, K. Xu, V. Murugesan and K. T. Mueller, Origin of Unusual Acidity and Li^+ Diffusivity in a Series of Water-in-Salt Electrolytes., *J. Phys. Chem. B,* 2020, **124,** 5284-5291.

[9] J. Jeon, H. Lee, J.-H. Choi, and M. Cho, Modeling and Simulation of Concentrated Aqueous Solutions of LiTFSI for Battery Applications, *J. Phys. Chem. C* 2020, **124,** 11790–11799.

[10] N.H. C. Lewis, Y. Zhang, B. Dereka, E. V. Carino, E. J. Maginn, and A. Tokmakoff, Signatures of Ion Pairing and Aggregation in the Vibrational Spectroscopy of Super-Concentrated Aqueous Lithium Bistriflimide Solutions, *J. Phys. Chem. C,* 2020, **124,** 3470–3481.

[11] Y. Zhang, N. H. C. Lewis, J. Mars, G. Wan, N. J. Weadock, C. J. Takacs, M. R. Lukatskaya, H.-G. Steinrück, M. F. Toney, A. Tokmakoff and E. J. Maginn, Water-in-Salt LiTFSI Aqueous Electrolytes. 1. Liquid Structure from Combined Molecular Dynamics Simulation and Experimental Studies, *J. Phys. Chem. B,* 2021, **125,** 4501–4513.

[12] C. A. Angell, C. Liu and E. Sanchez, Rubbery Solid Electrolytes with Dominant Cationic Transport and High Ambient Conductivity, *Nature,* 1993, **362**, 137−139.

[13] Y. Zhang and E. J. Maginn, Water-In-Salt LiTFSI Aqueous Electrolytes (2): Transport Properties and Li^+ Dynamics Based on Molecular Dynamics Simulations, *J. Phys. Chem. B,* 2021, **125**, 48, 13246–13254.

[14] M. A. González, O. Borodin, M. Kofu, K. Shibata, T. Yamada, O. Yamamuro, K. Xu, D. L. Price and M.-L. Saboungi, Nanoscale Relaxation in "Water-in-Salt" and "Water-in-Bisalt" Electrolytes, *J. Phys. Chem. Lett.,* 2020, **11**, 7279−7284.

[15] Y. S. Badyal, D. L. Price, M.-L. Saboungi, D. R. Haeffner and S. D. Shastri, Quantum effects on the structure of water at constant temperature and constant atomic density, *J. Chem. Phys.,* 2002, **116**, 10833-10837.

[16] G. Horwitz, E. Härk, P. Y. Steinberg, L. P. Cavalcanti, S. Risse, and H. R. Corti, The Nanostructure of Water-in-Salt Electrolytes Revisited: Effect of the Anion Size, *ACS Nano,* 2021, **15,** 11564-11572.

[17] H. E. Fischer, G. J. Cuello, P. Palleau, D. Feltin, A. C. Barnes, Y. S. Badyal and J. M. Simonson, D4c: A very high precision diffractometer for disordered materials, *Appl. Phys. A*, 2002, **74**, S160-S162.

[18] J. R. Stewart, P. P. Deen, K. H. Andersen, H. Schober, J.-F. Barthélemy, J. M. Hillier, A. P. Murani, T. Hayes, and B. Lindenau, Disordered materials studied using neutron polarization analysis on the multi-detector spectrometer D7, *J. Appl. Cryst.,* 2009, **42,** 69-84 .

[19] M.-L. Saboungi, G. J. Cuello, A. Dobosz, M. A. González, L. Hennet, L. Mangin-Thro, D. L. Price and O. Yamamuro, Water Structure In 'Water-In-Salt'and 'Water-In-Bisalt' Electrolytes, 2019, *Institut Laue-Langevin (Ill).* doi:10.5291/Ill-Data.6-02-593

[20] M. A. González and L. Mangin-Thro, Water Structure In 'Water-In-Salt'and 'Water-In-Bisalt' Electrolytes, 2020, *Institut Laue-Langevin (Ill).* doi: 10.5291/Ill-Data.Easy-633

[21] D. Richard, M. Ferrand and G. J. Kearley, Analysis and visualization of neutron-scattering data, *J. Neut. Res.,* 1996, **4**, 33-39.

[22] H. E. Fischer, A. C. Barnes, and P. S. Salmon, Neutron and x-ray diffraction studies of liquids and glasses, *Rep. Prog. Phys.,* 2006, **69**, 233-299.

[23] T. E. Faber and J. M. Ziman, A theory of the electrical properties of liquid metals, III. the resistivity of binary alloys, *Philos. Mag.,* 1965, **11**, 153-173.

[24] V. F. Sears, Neutron scattering lengths and cross sections, *Neutron News,* 1992, **3**, 26-37.

[25] S. Kohara, M. Itou, K. Suzuya, Y. Inamura, Y. Sakurai, Y. Ohishi and M. Takata, Structural studies of disordered materials using high-energy x-ray diffraction from ambient to extreme conditions, *J. Phys.: Condes. Matter,* 2007, **19**, 506101.

[26] K. Ohara, Y. Onodera, M. Murakami and S. Kohara, Structure of disordered materials under ambient to extreme conditions revealed by synchrotron x-ray diffraction techniques at SPring-8—recent instrumentation and synergic collaboration with modelling and topological analyses, *J. Phys.: Condens. Matter,* 2021, **33**, 383001.

[27] O. Borodin, Polarizable Force Field Development and Molecular Dynamics Simulations of Ionic Liquids, *J. Phys. Chem. B*, 2009, **113**, 11463-11478.

[28] O. Borodin, G. A. Giffin, A. Moretti, J. B. Haskins, J. W. Lawson, W. A. Henderson and S. Passerini, Insights into the Structure and Transport of the Lithium, Sodium, Magnesium, and Zinc Bis(trifluoromethansulfonyl)imide Salts in Ionic Liquids, *J. Phys. Chem. C*, 2018, **122**, 20108-20121.

[29] O. N. Starovoytov , Borodin O, Bedrov D, & Smith GD (2011) Development of a Polarizable Force Field for Molecular Dynamics Simulations of Poly (Ethylene Oxide) in Aqueous Solution. *J. Chem. Theory Comput.* 7(6):1902-1915.

[30] S. Plimpton, Fast Parallel Algorithms for Short-Range Molecular Dynamics, *J. Comp. Phys.,* 1995, **117**, 1-19.

[31] W. L. Jorgensen, D. S. Maxwell and J. Tirado-Rives, Development and Testing of the OPLS All-Atom Force Field on Conformational Energetics and Properties of Organic Liquids, *J. Am. Chem. Soc.* 1996, **118,** 11225–11236.

[32] J. Wang, R. M. Wolf, J. W. Caldwell, P. A. Kollman and D. A. Case, Development and testing of a general amber force field. *J. Comp. Chem.,* 2004, **25**, 1157-1174

[33] Y. Wu, H. L Tepper and G. A. Voth, Flexible simple point-charge water model with improved liquid-state properties, *J. Chem. Phys.,* 2006, **124**, 024503.

[34] Y. Zhang and E. J. Maginn, A Simple AIMD Approach to Derive Atomic Charges for Condensed Phase Simulation of Ionic Liquids, *J. Phys. Chem. B,* 2012, **116**, 10036–10048.

[35] R. W. Hockney, Computer Simulation Using Particles, Adam Hilger, New York, 1989.

[36] H. Sun, COMPASS: An ab Initio Force-Field Optimized for Condensed-Phase Applications - Overview with Details on Alkane and Benzene Compounds, *J. Phys. Chem. B,* 1998, **102**, 7338–7364.

[37] W. G. Hoover, Canonical dynamics: Equilibrium phase-space distributions, *Phys. Rev. A***,** 1985, **31**, 1695-7.

[38] W. Shinoda, M. Shiga, and M. Mikami, Rapid estimation of elastic constants by molecular dynamics simulation under constant stress*, Phys. Rev. B*, 2004, **69**, 134103.

[39] J. C. Araque, J. J. Hettige, and C. J. Margulis, Modern room temperature ionic liquids, a simple guide to understanding their structure and how it may relate to dynamics, *J. Phys. Chem. B*, 2015, **119**, 12727-12740.

[40] M. Tomšič, A. Jamnik, G. Fritz-Popovski, O. Glatter, L. Vleček, Structural properties of pure simple alcohols from ethanol, propanol, butanol, pentanol, to hexanol: Comparing Monte Carlo simulations with experimental SAXS data, *J. Phys. Chem. B,* 2007, **111**, 1738-1751.

[41] A. Perera, Charge ordering and scattering pre-peaks in ionic liquids and alcohols, *Phys. Chem. Chem. Phys.,* 2017, **19**, 1062-1073.

[42] O. Borodin, D. L. Price, B. Aoun, M. A. González, J. B. Hooper, M. Kofu, S. Kohara, Osamu Yamamuro and M.-L. Saboungi, Effect of water on the structure of a prototype ionic liquid, *Phys. Chem. Chem. Phys*., 2016, **18,** 23474-23481.

[43] O. Borodin, W. Gorecki, G. D. Smith and M. Armand, Molecular Dynamics Simulation and Pulsed-Field Gradient NMR Studies of Bis(fluorosulfonyl)imide (FSI) and Bis[(trifluoromethyl)sulfonyl]imide (TFSI) Based Ionic Liquids, *J. Phys. Chem. B*, 2010, **114**, 6786–6798.